Demonstrating the Ultrathin Metal–Insulator–Metal Diode Using TiN/ZrO$_2$–Al$_2$O$_3$–ZrO$_2$ Stack by Employing RuO$_2$ Top Electrode

Woojin Jeon [ID], Youngjin Kim, Cheol Hyun An, Cheol Seong Hwang, Patrice Gonon, and Christophe Vallée

Abstract— **Metal–insulator–metal (MIM) diodes with ultrathin insulators are highly promising for a variety of applications, such as vertical integration technology. However, MIM diodes with thin enough structures have not been achieved in previous studies on diodes using Schottky emission or tunneling conduction asymmetry. In this paper, we demonstrate an MIM diode with an ultrathin, 5-nm ZrO$_2$/Al$_2$O$_3$/ZrO$_2$ insulator, using the work-function difference between the top and bottom electrodes. The rectifying properties of the diode were enhanced by employing RuO$_2$ as an electrode, due to its high work function and the catalytic effect on oxygen decomposition, contributing to the suppression of trap-assisted tunneling. This paper presents an important development in understanding MIM structures with respect to the electrical and chemical properties.**

Index Terms— **Capacitance–voltage (C–V) nonlinearity, catalytic effect, metal–insulator–metal (MIM) diode, oxygen vacancy, trap-assisted tunneling (TAT), work-function difference.**

I. INTRODUCTION

VERTICAL integration is a critical attribute for the future development of semiconductor devices, as it addresses the limitations of patterning [1]–[4]. Reducing the total thickness of each component is crucial to the success of vertical integration. Hence, minimizing the thickness of a metal–insulator–metal (MIM) diode, which has recently attracted significant attention for application in electronic devices such as infrared photodetectors [5]–[8], rectennas for energy harvesting [9]–[11], hot electron transistors [12], [13], high-frequency mixers [14], [15], and selectors or switching components in semiconductor memory [16]–[21], is necessary. Especially, the concept of vertical integration has attracted much attention, particularly in the study of semiconductor memory; however, there is a new limitation associated with this technique; the total thickness of a full stack, i.e., the stack height in the conventional planar integration, is limited by the design rule [4]. Thinner elements are thus more favorable for vertical integration. Moreover, thinner elements are advantageous for the development of a competitive fabrication process, with respect to factors such as cost and time. In [16], [17], [22]–[25], and [26], high asymmetry (f_{ASYM}) and nonlinearity (f_{NL}) were obtained in the current density–voltage (J–V) curves of MIM diodes based on Schottky emission or tunneling conduction asymmetry. These properties were attributed to differences in the work function of the electrodes [20]–[22], [26], [27] or to the bilayer insulator structure [22], [26]. However, the insulator in an MIM diode based on Schottky-emission processes should be thick enough to prevent dielectric breakdown. The asymmetry from the tunneling current decreases in line with the thickness of the insulator, due to the increased tunneling probability in both directions [22], [26], making the construction of MIM diodes capable of vertical integration difficult.

Of the various high-k dielectric materials available, an insulator consisting of a ZrO$_2$/Al$_2$O$_3$/ZrO$_2$ (ZAZ) stacked structure has been widely used as the dielectric for dynamic random access memory capacitors, because this structure has a low-leakage current density even when it is only a few nanometers thick [28]–[30]. Accordingly, ZAZ is a suitable insulator for extremely thin MIM diodes (e.g., <10 nm). Consequently, we have demonstrated an MIM diode consisting of an extremely thin 5-nm ZAZ insulator, and 10-nm TiN and 5-nm RuO$_2$ as bottom electrode (BE) and top electrode (TE), respectively, which exhibited an f_{ASYM} of 228.7 and an f_{NL} of 13.6. This paper also presents related mechanisms for explaining the enhanced rectifying properties of an MIM diode, based on various electrical and chemical analyses.
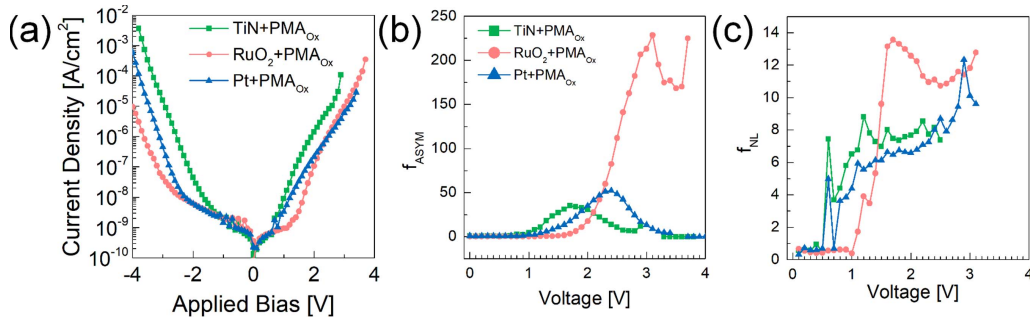
Fig. 1. (a) J–V curves of MIM structures consisted of TiN for BE, 5-nm-thick ZAZ for insulator, and TiN (blue), RuO_2 (green), and Pt (red) for TE, respectively. The J–V curve measurement was performed after employing PMA_{Ox}. (b) f_{ASYM} versus V and (c) f_{NL} versus V plots for the MIM structure with TiN, RuO_2, and Pt TE from the J–V curves measured in (a).

II. EXPERIMENTAL PROCEDURES

To fabricate the MIM diode, a ZAZ film was deposited on a substrate comprising 10 nm of sputtered TiN, acting as a BE, on a thermally oxidized (100) Si wafer. The ZrO_2 and Al_2O_3 layers were deposited on the substrate using atomic layer deposition (ALD), with Tetrakis–ethylmethylamino–zirconium [$Zr(N-(CH_3)(C_2H_5))_4$, TEMAZ] and trimethylalu-minum [$(CH_3)_3Al$, TMA] as precursors, and O_3 as an oxidant, respectively. The process temperature was 250 °C. The thickness of the ZAZ stack was controlled to 5 nm. A desirable current density was obtained using a film stacked from bottom to top with ZrO_2, Al_2O_3, and ZrO_2, at thicknesses of 2, 1.5, and 1.5 nm, respectively. The materials in the TE (TiN, Pt, and RuO_2) were deposited as follows: 5-nm-thick TiN and 30-nm-thick Pt were deposited using radio frequency (RF) sputtering in Ar/N_2 atmosphere and in Ar atmosphere, respectively. The 5-nm-thick RuO_2 layer was deposited using dc reactive sputtering in Ar/O_2 atmosphere. An additional 30-nm-thick Pt layer was deposited on the TiN and RuO_2 layers, to improve probing contact during the electrical measurement. The deposition conditions for the TE were carefully optimized, to minimize the sputter-damage effect on the insulator layer, which has been reported elsewhere in [31]. Following TE deposition, we performed different postmetallization annealing (PMA) processes, including oxygen-promoted annealing (PMA_{Ox}) in 95%:5% N_2/O_2 atmosphere, at 400 °C for 30 min, and oxygen-prohibited annealing (PMA_N) in N_2, at 400 °C for 30 min, using a tube furnace.

The film thicknesses were measured via spectroscopic ellipsometry (J. A. Woollam, ESM-300), X-ray fluorescence (Thermo Scientific, ARL Quant'X), and X-ray reflection (PANalytical, X'Pert Pro). The chemical composition of the film was characterized using X-ray photoemission spectroscopy (XPS, Thermo Fisher, theta 300) and time-of-flight secondary ion mass spectrometry (ToF-SIMS, Cameca, IMS-4FE7). To fabricate a testing cell for measurement of the electrical properties of the fabricated device, the TE was defined using a metal shadow mask, with a 300-μm-diameter hole. Adhesive indium paste was applied to the side of the sample to create contact with the TiN layer of the BE. The electrical performance of the fabricated device was studied by measuring the capacitance–voltage (C–V) and the J–V curves, using a picoammeter/dc voltage source

TABLE I
SUMMARY OF THE VALUES EXTRACTED FROM THE ELECTRICAL MEASUREMENTS FOR EVALUATING THE DIODE CHARACTERISTICS AND C–V NONLINEARITY

		TiN	RuO_2	Pt
f_{ASYM}	PMA_{Ox}	35.2	228.7	52.3
f_{NL}	PMA_{Ox}	8.8	13.6	~6
α ($\times10^{-2}$ V^{-2})	PMA_{Ox}	7.77	0.500	5.84
	PMA_N	3.42	2.59	11.2

(Hewlett Packard 4140D), and an impedance analyzer (Hewlett Packard 4194A). The ac excitation bias and frequency used in C–V measurement were 0.02 V and 10 kHz, respectively. The TE was biased, and the BE was grounded, during the electrical tests.

III. RESULTS AND DISCUSSION

A. Current–Voltage Characteristics

The diode characteristics, i.e., the J–V, f_{ASYM} versus voltage and f_{NL} versus voltage curves, relating to the TE were investigated, as shown in Fig. 1. A PMA_{Ox} treatment was performed with all the samples, as described in experimental section. As f_{ASYM} is defined as positive current density divided by negative current density, or $|J_+/J_-|$, $f_{ASYM} = 1$ indicates no rectification. f_{NL} is defined as the ratio of the differential conductance to the conductance, $(dJ/dV)/(J/V)$. With a TiN TE, the MIM structure had an asymmetric J–V curve, where the maximum value of f_{ASYM} was 35.2 at +1.7 V. The values extracted from electrical measurement of all the samples are summarized in Table I. The current density in the negative sweep direction was higher with the TiN sample than with either the RuO_2 sample or the Pt sample, due to the lower work function of TiN. Even though there is no work-function difference between the TE and BE, the current density in the positive sweep direction is relatively higher than that in the negative sweep direction, creating some asymmetry (f_{ASYM}), possibly due to the degradation of the interface between the TiN BE and the ZrO_2 film [32]–[34],

as will be discussed in Section III-C. However, this MIM structure, which has the same metal in the TE and BE, is limited in its ability to increase f_{ASYM}. The value of f_{ASYM} was increased significantly with the RuO$_2$ TE and the Pt TE, where they were 228.7 and 52.3, at +3.1 and +2.4 V, respectively. While the work function of RuO$_2$ is lower than that of Pt, the MIM structure with the RuO$_2$ TE had a higher value of f_{ASYM} than the structure with the Pt TE. Moreover, with the RuO$_2$ TE sample, the slope of the f_{NL}–V plot was significantly increased when the applied bias was approximately +1 V, where f_{ASYM} begins to increase. However, similar f_{NL} behavior was not observed with the TiN TE and Pt TE samples.

To evaluate why the RuO$_2$ TE sample demonstrated higher values of f_{ASYM} and f_{NL}, we investigated the differences between the J–V curves of the TiN TE, RuO$_2$ TE, and Pt TE samples. First, we observed that in the negative bias sweep condition, the current density of the RuO$_2$ TE sample was lower than that of the TiN TE and Pt TE samples. The slope of the J–V curve in the negative sweep direction significantly increased at an applied bias of approximately −1.2 V, in the case of the TiN TE, whereas this increase was observed at approximately −2.5 V in the case of the RuO$_2$ and Pt TEs. This is because electrons are injected from the TE when a negative bias is applied, meaning that the difference in electron injection observed in the negative sweep condition depends on the work-function differences of the TEs, which are 4.6, 5.1, and 5.6 eV, for TiN, RuO$_2$, and Pt samples, respectively. However, in the negative sweep direction, the slope of the J–V curve of the RuO$_2$ TE sample was much lower than that of the Pt TE sample, even though the work function of RuO$_2$ is lower than the work function of Pt. It appears that this result is caused by Fermi-level pinning at the interface of the Pt TE and the ZrO$_2$ film. Fermi-level pinning is typically observed in MIM structures with high-k dielectrics and metal electrodes [35]–[38]. The Fermi level of the metal electrode is pinned to traps in the band gap of the high-k dielectric, lowering the effective work function of the metal electrode [35], [37]. The RuO$_2$ TE is more favorable than the Pt TE with respect to Fermi-level pinning, as activated oxygen is used in its fabrication, which can annihilate traps in a high-k dielectric. This trap annihilation induces the lower current density observed with the RuO$_2$ TE sample.

The J–V curves collected in the positive sweep condition also exhibited different behaviors with respect to the TE materials. In this condition, electrons are injected from the BE. Therefore, the fact that all the samples employ TiN in the BE causes less of a difference between the current density of the samples, compared with the negative bias sweep condition. However, we observed a significant difference in the J–V curves of the RuO$_2$ TE and Pt TE samples. Whereas the magnitude of the current density and the slope of J–V curves were identical at applied biases above +2 V, we noted, from the J–V curve of the RuO$_2$ TE sample, a lower current density than the Pt TE sample, for applied biases below +2 V, where the slope of the J–V curve changes. These features in the J–V curve of the RuO$_2$ TE sample explain the enhanced MIM diode properties, with respect to f_{ASYM} and f_{NL}.
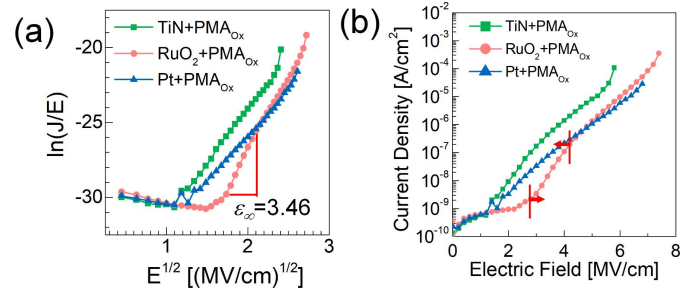
Fig. 2. (a) ln(J/E) versus $E^{1/2}$ plots of the MIM structure with TiN, RuO$_2$, and Pt TE to confirm the Poole–Frenkel emission mechanism. The red lines indicate the well-fitted region for RuO$_2$ + PMA$_{Ox}$ sample where exhibits linearity with adequate optical dielectric constant extracted from (1). (b) J–E curves of the MIM structure with TiN TE, RuO$_2$ TE, and Pt TE to show the region where the current flow is well fitted with the Poole–Frenkel emission mechanism, indicating with the red lines. The well-fitted region is only observed in RuO$_2$ + PMA$_{Ox}$ sample.

The differences in the J–V curves of the RuO$_2$ TE and Pt TE samples, following a positive sweep, were further investigated with respect to current conduction. There are three current conduction mechanisms for MIM structures that use ZrO$_2$ as the insulator: trap-assisted tunneling (TAT), Poole–Frenkel (P–F) emission, and Fowler–Nordheim (F–N) tunneling [30], [39]–[44]. F–N tunneling depends on the barrier height created by the work-function difference at the interface of the metal electrode and the insulator, and affects current conduction in relatively high electric field (E-field) regions. The similarity in the J–V curves of the RuO$_2$ TE and Pt TE samples at applied biases above +2 V is thus consistent with the features of F–N tunneling, as both samples have a similar interface between the TiN BE and the ZrO$_2$ layer. Moreover, the fact that the differing behavior was observed in a low applied bias region (below 2 V) indicates that TAT and P–F emission dictate the differences in the J–V curves [30], [39]. To quantitatively explain differences in the low bias region and the relative contribution of each conduction mechanism, the J–V curves for TiN TE, RuO$_2$ TE, and Pt TE samples were plotted in P–F emission coordinates, in Fig. 2(a), according to the following equation:

$$J \propto E \exp\left(\frac{-q\left(\phi_B - \sqrt{qE/(\pi\varepsilon_0\varepsilon_\infty)}\right)}{k_B T}\right) \quad (1)$$

where J, E, q, ϕ_B, ε_0, ε_∞, k_B, and T are the current density, applied E-field, elementary charge, barrier height, vacuum permittivity, optical dielectric constant, Boltzmann's constant, and temperature, respectively. According to (1), the slope of the linear regression region in each graph gives the optical dielectric constant (ε_∞). From the value of ε_∞ calculated, only the RuO$_2$ sample displayed behavior consistent with the P–F emission mechanism, in the region defined by the bias point, where the slope of the J–V curve starts to increase, to the bias point where the current density of the RuO$_2$ TE sample and the Pt TE sample coincide. The shape of the J–V plot, and the E-field in the "well-fitted" P–F emission region, indicated with red lines in Fig. 2(b), is consistent with the previous results [39], [40]. However, no region with an appropriate value of ε_∞ is observed in the plots of the TiN TE and Pt
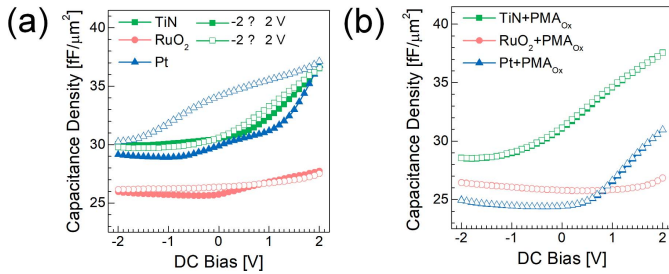
Fig. 3. $C-V$ curves of the MIM structure with TiN TE, RuO_2 TE, and Pt TE at (a) as-deposition state of TE and (b) after employing PMA_{Ox} state, respectively. The closed and opened symbols indicate the dc bias sweep direction of -2 to $+2$ V and $+2$ to -2 V in a single test cell, respectively.

Fig. 5. Zr 3d XPS spectra of ZAZ/TiN(BE) (black), RuO_2(TE)/ZAZ/TiN(BE) at as-deposited state (gray), RuO_2(TE)/ZAZ/TiN(BE) with PMA_{Ox} (red), and RuO_2(TE)/ZAZ/TiN(BE) with PMA_N (blue).
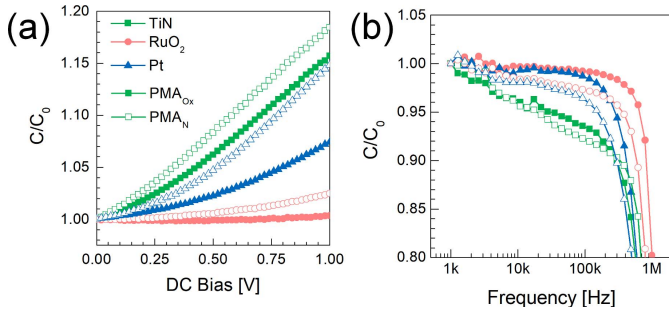
Fig. 4. Plots of (a) C/C_0 versus dc bias and (b) C/C_0 versus frequency for the MIM structure with TiN TE, RuO_2 TE, and Pt TE. The closed and opened symbols in both (a) and (b) indicate after employing PMA_{Ox} and PMA_N states, respectively.

TE samples, indicating that another mechanism contributed to current conduction, simultaneously. The likeliest of these mechanisms is TAT, as it is also functional in low E-field regions [39]. Hence, the result of P–F emission fitting suggests the suppression of TAT at the interface of the TiN BE and ZrO_2 in the RuO_2 sample.

B. Capacitance–Voltage Characteristics

To investigate changes in the trap density of the MIM structure, we performed analysis of the $C-V$ curve. Fig. 3 shows the $C-V$ curves of MIM structures with TiN TE, RuO_2 TE, and Pt TE in an as-deposited state, and following a PMA_{Ox} treatment. We observed large hysteresis in the $C-V$ curves of the TEs in the as-deposited state, possibly originating from sputtering damage, which occurs during the deposition of the TE. The $C-V$ curve of the Pt TE sample had significantly larger hysteresis compared to the curves of the RuO_2 and TiN samples, caused by the differing sputtering conditions. We also observed severe negative curvature in the $C-V$ nonlinearity in the positive dc bias region, i.e., the dependence of the capacitance density (C) on the dc bias (V). While the hysteresis in the $C-V$ curve disappears following the PMA_{Ox} treatment, the $C-V$ nonlinearity is still observed. We observed a decrease in capacitance density in only the Pt TE sample. We suggest that this decrease is related to either the large hysteresis in the as-deposition state or originates from the chemical or structural transitions of Pt during the PMA_{Ox} process [45]. The dc-bias-dependent (V) relative capacitance (C/C_0, where C_0 is the capacitance at zero dc bias) curves for the PMA_{Ox} samples are shown in Fig. 4(a)
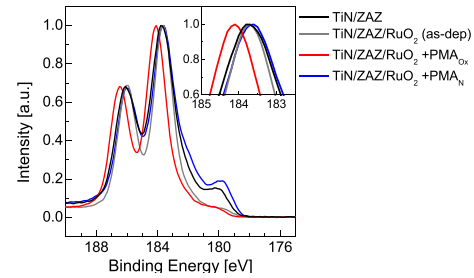
to determine the dependence of the $C-V$ nonlinearity on the composition of the TE. The C/C_0-V curves of the PMA_{Ox}-treated samples show an opposite trend. In contrast to the TiN and conducting PMA_{Ox} (TiN + PMA_{Ox}) sample, and the Pt and conducting PMA_{Ox} (Pt + PMA_{Ox}) sample, no dependence of C/C_0 on dc bias was observed with the RuO_2 and conducting PMA_{Ox} (RuO_2 + PMA_{Ox}) sample. Moreover, for the RuO_2 + PMA_{Ox} sample, the quadratic voltage coefficient of the capacitance (α), which is derived from the expression, $C/C_0 = 1 + \beta V + \alpha V^2$, where β is the linear voltage coefficient of the capacitance, was calculated to be 0.005 V^{-2}. For TiN + PMA_{Ox} and Pt + PMA_{Ox} samples, α was calculated to be 0.07765 and 0.05837 V^{-2}, respectively. Hence, this opposite trend in the $C-V$ nonlinearity implies that defects (or traps) in the MIM structure, which induce the dependence of C/C_0 on the dc bias, are not formed in the processing of the RuO_2 + PMA_{Ox} sample. The $C-V$ nonlinearity can be explained using the Maxwell–Wagner space charge polarization (also called electrode polarization) model [18], [46]–[48]. According to the electrode polarization mechanism, $C-V$ nonlinearity depends on a hopping carrier, through ionic conduction of an oxygen vacancy (V_O) (migration of oxygen vacancies) or localized electronic conduction (electronic hopping between vacancy sites). The plot of the dependence of ac frequency on the TE [Fig. 4(b)] also indicates the different contributions of electrode polarization to the capacitance of the TE, since carrier hopping decreases with increasing ac frequency. The trend in this plot complements the trend observed in $C-V$ nonlinearity, suggesting that the defect causing the $C-V$ nonlinearity depends on the TE. The comparatively high $C-V$ nonlinearity of the TiN + PMA_{Ox} sample indicates that the V_O in ZrO_2, from the formation of TiO_x (or TiO_xN_y), which originates from the reaction of ZrO_2 and TiN, causes the $C-V$ nonlinearity, since the TiN + PMA_{Ox} sample has two interfaces of ZrO_2 and TiN, at the TE and the BE, respectively.

However, the RuO_2 + PMA_{Ox} sample exhibited extremely low $C-V$ nonlinearity, even though, as with the Pt + PMA_{Ox} sample, the RuO_2 + PMA_{Ox} sample has a ZrO_2/TiN interface at the BE. This differing behavior can be explained by the catalytic effect of RuO_2. The RuO_2 layer acts as a catalyst for oxygen decomposition because of its oxidation–reduction reaction characteristics [46]. This feature contributes to the enhanced growth rate of the TiO_2 film deposition using the ALD technique [49], [50]. The catalytic decomposition
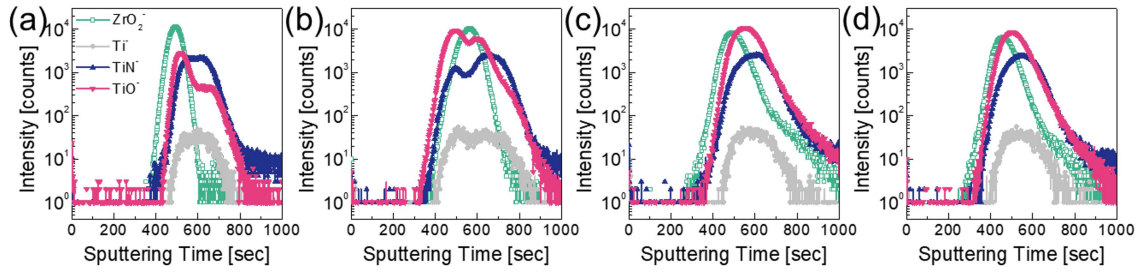
Fig. 6. SIMS analyses of the MIM structure with TiN for BE, 5-nm-thick ZAZ for insulator, and (a) RuO_2 TE at as-deposited state, (b) TiN TE after employing PMA_{Ox}, (c) RuO_2 TE after employing PMA_{Ox}, and (d) Pt TE after employing PMA_{Ox}.

of RuO_2, with the help of the Ru in the film, increases the magnitude of active oxygen, enhancing the growth rate of the TiO_2 film, through the reaction between the active oxygen and the adsorbed Ti precursor. The RuO_2 TE induces the decomposition of oxygen in atmosphere during the PMA_{Ox} process, and supplies active oxygen atoms to the MIM structure, resulting in the decreased V_O density in the ZrO_2 layer. The TAT suppression in the RuO_2 + PMA_{Ox} sample can also be explained by the decreased V_O density in the ZrO_2 layer, as the dominant trap contributing to TAT at the TiN/ZrO_2 interface is the V_O in ZrO_2 [43]. Hence, the reduced contribution of TAT to current conduction in the positive sweep condition of the RuO_2 TE sample is due to a combination of the PMA_{Ox} process and the RuO_2 TE. However, the value of α in the C/C_0–V plot of the PMA_N-treated RuO_2 TE sample (RuO_2 + PMA_N) is 2.59, which is higher than that of the RuO_2 + PMA_{Ox} sample (Table I). We also note greater dependence of C/C_0 on ac frequency with the RuO_2 + PMA_N sample, compared with the RuO_2 + PMA_{Ox} sample. These results indicate that the RuO_2 TE acts solely as a catalyst, and the oxygen atoms for annihilating V_O originate from O_2 in the atmosphere during the PMA_{Ox} process.

C. Chemical Analysis

To characterize the chemical state of the films, XPS and SIMS analyses were conducted (Figs. 5 and 6). Prior to performing XPS measurements, Ar-ion beam etching was employed on the top surface of the sample, for clearer measurement of the chemical state of the ZrO_2 layer at the interface of the TiN BE. Fig. 5 shows XPS spectra of the 3d core levels of Zr for a ZAZ/TiN(BE) sample, a sample with $RuO_2(TE)/ZAZ/TiN(BE)$ in the as-deposited state, a PMA_{Ox}-treated $RuO_2(TE)/ZAZ/TiN(BE)$ sample, and a PMA_N-treated $RuO_2(TE)/ZAZ/TiN(BE)$ sample. The Zr 3d XPS spectra of the four samples are composed of Zr $3d_{5/2}$ peaks centered at binding energies of ~184 and 179.8 eV, which correspond to the energies of ZrO_2 and metallic Zr, respectively. The metallic Zr is probable induced by the damage from employed Ar-ion etching. In the cases of the ZAZ/TiN(BE) sample, the sample with $RuO_2(TE)/ZAZ/TiN(BE)$ in the as-deposited state, and the PMA_N-treated $RuO_2(TE)/ZAZ/TiN(BE)$ sample, the Zr peak corresponding to ZrO_2 was observed at ~183.7 eV, indicating that the reaction between the TiN BE and ZrO_2 induces a ZrO_{2-x} phase during ALD of the ZrO_2 layer [39], [51]. Moreover, the binding energy of the peak

corresponding to ZrO_2 in the XPS spectrum of the PMA_{Ox}-treated $RuO_2(TE)/ZAZ/TiN(BE)$ sample was 184.1 eV, which is consistent with stoichiometric ZrO_2, revealing that the ZrO_{2-x} is reoxidized by ambient O_2 and the catalytic effect of the RuO_2 TE [49]. Consequently, when a PMA_{Ox}-treated RuO_2 TE is employed, the electrical characteristics related to the V_O are significantly reduced. We examined the chemical state and depth profile of TiN and TiO_x using SIMS analysis, as this technique can detect the presence of oxidized TiN regardless of its chemical state (TiO_x or TiO_xN_y), and provide depth-profile information without severe degradation to the sample through sources such as the electron charging effect, which might be induced during ion sputtering. In Fig. 6(a), the intensity curve corresponding to TiO^- ions, collected from a sample following deposition of the RuO_2 TE, exhibited a peak located at the interface of ZrO_2 and TiN BE, possibly originating from oxidation during the ZrO_2 deposition process. The TiO^- curve of the remaining samples, following PMA_{Ox} treatment [Fig. 6(b)–(d)], were broad, with a high intensity, indicating that a reaction occurs between ZrO_2 and the TiN film during the PMA_{Ox} process. Two peaks were observed in the TiO^- curve of the TiN + PMA_{Ox} sample, at the interfaces of the TE/insulator and the BE/insulator, respectively. The lack of a significant difference in the TiO^- curve of the RuO_2 + PMA_{Ox} sample, compared to the curve of the Pt + PMA_{Ox} sample, suggests that the formation of TiO_x depends on the thermal energy of the PMA process, and not on the deposition of the TE.

IV. CONCLUSION

An MIM diode with an extremely thin stack, consisting of a 10-nm-thick TiN, 5-nm-thick ZAZ, and 5-nm-thick RuO_2, was demonstrated, and mechanisms explaining the rectifying property of the device were investigated. The higher f_{ASYM} of the RuO_2 TE sample was achieved by a decrease in the current density of the negative bias sweep, owing to the higher work-function of RuO_2, and a lack of Fermi-level pinning. Moreover, the electrical property of the interface between the TiN BE and the ZrO_2 layer is affected by the TE. In the case of the RuO_2 + PMA_{Ox} sample, the V_O in ZrO_2, at the interface with the TiN BE, was effectively annihilated as a result of the catalytic effect of RuO_2 on oxygen decomposition, inducing an improvement in C–V nonlinearity and suppression of TAT. The XPS results also confirmed the dependence of the ZrO_{2-x} ratio on the PMA condition.

REFERENCES

[1] C. S. Hwang, S. K. Kim, and S. W. Lee, "Mass-production memories (DRAM and Flash)," in *Atomic Layer Deposition for Semiconductors*. Boston, MA, USA: Springer, 2014, pp. 73–122, doi: 10.1007/978-1-4614-8054-9_4.

[2] Y. Fukuzumi *et al.*, "Optimal integration and characteristics of vertical array devices for ultra-high density, bit-cost scalable flash memory," in *IEDM Tech. Dig.*, Dec. 2007, pp. 449–452, doi: 10.1109/IEDM.2007.4418970.

[3] K. Kim and G. Jeong, "Memory technologies for sub-40 nm node," in *IEDM Tech. Dig.*, Dec. 2007, pp. 27–30, doi: 10.1109/IEDM.2007.4418854.

[4] J. Kim *et al.*, "Novel Vertical-Stacked-Array-Transistor (VSAT) for ultra-high-density and cost-effective NAND flash memory devices and SSD (Solid State Drive)," in *Proc. Symp. VLSI Technol.*, Jun. 2009, pp. 186–187.

[5] P. C. D. Hobbs, R. B. Laibowitz, F. R. Libsch, N. C. LaBianca, and P. P. Chiniwalla, "Efficient waveguide-integrated tunnel junction detectors at 1.6 μm," *Opt. Exp.*, vol. 15, no. 25, pp. 16376–16389, Dec. 2007, doi: 10.1364/OE.15.016376.

[6] H. Chalabi, D. Schoen, and M. L. Brongersma, "Hot-electron photodetection with a plasmonic nanostripe antenna," *Nano Lett.*, vol. 14, no. 3, pp. 1374–1380, Mar. 2014, doi: 10.1021/nl4044373.

[7] F. Wang and N. A. Melosh, "Power-independent wavelength determination by hot carrier collection in metal-insulator-metal devices," *Nature Commun.*, vol. 4, Apr. 2013, Art. no. 1711, doi: 10.1038/ncomms2728.

[8] A. A. Khan, G. Jayaswal, F. A. Gahaffar, and A. Shamim, "Metal-insulator-metal diodes with sub-nanometre surface roughness for energy-harvesting applications," *Microelectron. Eng.*, vol. 181, pp. 34–42, Sep. 2017, doi: 10.1016/J.MEE.2017.07.003.

[9] E. G. Arsoy, M. Inac, A. Shafique, M. Ozcan, and Y. Gurbuz, "The metal-insulator-metal diodes for infrared energy harvesting and detection applications," *Proc. SPIE*, vol. 9819, p. 98190F, May 2016, doi: 10.1117/12.2224748.

[10] Shilpi, K. Bhatt, Sandeep, S. Kumar, and C. C. Tripathi, "Potential challenges and issues in implementation of MIM diodes for rectenna application," in *Proc. Int. Conf. Invent. Commun. Comput. Technol. (ICICCT)*, 2017, pp. 83–88, doi: 10.1109/ICICCT.2017.7975164.

[11] M. N. Gadalla, M. Abdel-Rahman, and A. Shamim, "Design, optimization and fabrication of a 28.3 THz nano-rectenna for infrared detection and rectification," *Sci. Rep.*, vol. 4, Mar. 2014, Art. no. 4270, doi: 10.1038/srep04270.

[12] C. Zeng *et al.*, "Vertical graphene-base hot-electron transistor," *Nano Lett.*, vol. 13, no. 6, pp. 2370–2375, Jun. 2013, doi: 10.1021/nl304541s.

[13] S. Vaziri *et al.*, "A graphene-based hot electron transistor," *Nano Lett.*, vol. 13, no. 4, pp. 1435–1439, Apr. 2013, doi: 10.1021/nl304305x.

[14] S. Rockwell *et al.*, "Characterization and modeling of metal/double-insulator/metal diodes for millimeter wave wireless receiver applications," in *Proc. IEEE Radio Freq. Integr. Circuits (RFIC) Symp.*, Jun. 2007, pp. 171–174, doi: 10.1109/RFIC.2007.380858.

[15] C. Fumeaux, W. Herrmann, F. K. Kneubühl, and H. Rothuizen, "Nanometer thin-film Ni–NiO–Ni diodes for detection and mixing of 30 THz radiation," *Infr. Phys. Technol.*, vol. 39, no. 3, pp. 123–183, Apr. 1998, doi: 10.1016/S1350-4495(98)00004-8.

[16] K. J. Yoon *et al.*, "Double-layer-stacked one diode-one resistive switching memory crossbar array with an extremely high rectification ratio of 10^9," *Adv. Electron. Mater.*, vol. 3, no. 7, p. 1700152, Jul. 2017, doi: 10.1002/aelm.201700152.

[17] B. Govoreanu, C. Adelmann, A. Redolfi, L. Zhang, S. Clima, and M. Jurczak, "High-performance metal-insulator-metal tunnel diode selectors," *IEEE Electron Device Lett.*, vol. 35, no. 1, pp. 63–65, Jan. 2014, doi: 10.1109/LED.2013.2291911.

[18] P. Gonon *et al.*, "Resistance switching in HfO$_2$ metal-insulator-metal devices," *J. Appl. Phys.*, vol. 107, no. 7, p. 74507, Apr. 2010, doi: 10.1063/1.3357283.

[19] D.-Y. Lee, T.-L. Tsai, and T.-Y. Tseng, "Unipolar resistive switching behavior in Pt/HfO$_2$/TiN device with inserting ZrO$_2$ layer and its 1 diode-1 resistor characteristics," *Appl. Phys. Lett.*, vol. 103, no. 3, p. 32905, Jul. 2013, doi: 10.1063/1.4816053.

[20] W. Lee *et al.*, "Atomic layer deposition of SrTiO$_3$ films with cyclopentadienyl-based precursors for metal–insulator–metal capacitors," *Chem. Mater.*, vol. 25, no. 6, pp. 953–961, Mar. 2013, doi: 10.1021/cm304125e.

[21] W. Y. Park *et al.*, "A Pt/TiO$_2$/Ti Schottky-type selection diode for alleviating the sneak current in resistance switching memory arrays," *Nanotechnology*, vol. 21, no. 19, p. 195201, May 2010, doi: 10.1088/0957-4484/21/19/195201.

[22] N. Alimardani and J. F. Conley, Jr., "Enhancing metal-insulator-insulator-metal tunnel diodes via defect enhanced direct tunneling," *Appl. Phys. Lett.*, vol. 105, no. 8, p. 82902, Aug. 2014, doi: 10.1063/1.4893735.

[23] G. H. Kim *et al.*, "32 × 32 crossbar array resistive memory composed of a stacked Schottky diode and unipolar resistive memory," *Adv. Funct. Mater.*, vol. 23, no. 11, pp. 1440–1449, Mar. 2013, doi: 10.1002/adfm.201202170.

[24] P. Periasamy *et al.*, "Metal–insulator–metal diodes: Role of the insulator layer on the rectification performance," *Adv. Mater.*, vol. 25, no. 9, pp. 1301–1308, Mar. 2013, doi: 10.1002/adma.201203075.

[25] R. Urcuyo, D. L. Duong, H. Y. Jeong, M. Burghard, and K. Kern, "High performance graphene–oxide–metal diode through bias-induced barrier height modulation," *Adv. Electron. Mater.*, vol. 2, no. 9, p. 1600223, Sep. 2016, doi: 10.1002/aelm.201600223.

[26] N. Alimardani and J. F. Conley, Jr., "Step tunneling enhanced asymmetry in asymmetric electrode metal-insulator-insulator-metal tunnel diodes," *Appl. Phys. Lett.*, vol. 102, no. 14, p. 143501, Apr. 2013, doi: 10.1063/1.4799964.

[27] E. W. Cowell, III, *et al.*, "Advancing MIM electronics: Amorphous metal electrodes," *Adv. Mater.*, vol. 23, no. 1, pp. 74–78, Jan. 2011, doi: 10.1002/adma.201002678.

[28] S. Y. Lee, J. Chang, Y. Kim, H. Lim, H. Jeon, and H. Seo, "Depth resolved band alignments of ultrathin TiN/ZrO$_2$ and TiN/ZrO$_2$-Al$_2$O$_3$-ZrO$_2$ dynamic random access memory capacitors," *Appl. Phys. Lett.*, vol. 105, no. 20, p. 201603, Nov. 2014, doi: 10.1063/1.4902244.

[29] H. J. Cho *et al.*, "New TIT capacitor with ZrO$_2$/Al$_2$O$_3$/ZrO$_2$ dielectrics for 60 nm and below DRAMs," *Solid. State. Electron.*, vol. 51, nos. 11–12, pp. 1529–1533, Nov. 2007, doi: 10.1109/ESSDER.2006.307659.

[30] W. Weinreich *et al.*, "Detailed leakage current analysis of metal–insulator–metal capacitors with ZrO$_2$, ZrO$_2$/SiO$_2$/ZrO$_2$, and ZrO$_2$/Al$_2$O$_3$/ZrO$_2$ as dielectric and TiN electrodes," *J. Vac. Sci. Technol. B, Microelectron. Process. Phenom.*, vol. 31, no. 1, p. 01A109, Jan. 2013, doi: 10.1116/1.4768791.

[31] H. K. Kim, I.-H. Yu, J. H. Lee, T. J. Park, and C. S. Hwang, "Controlling work function and damaging effects of sputtered RuO$_2$ gate electrodes by changing oxygen gas ratio during sputtering," *ACS Appl. Mater. Interfaces*, vol. 5, no. 4, pp. 1327–1332, Feb. 2013, doi: 10.1021/am302604e.

[32] B. Sun *et al.*, "The effect of current compliance on the resistive switching behaviors in TiN/ZrO$_2$/Pt memory device," *Jpn. J. Appl. Phys.*, vol. 48, no. 4, p. 04C061, Apr. 2009, doi: 10.1143/JJAP.48.04C061.

[33] J.-H. Kim, V. A. Ignatova, J. Heitmann, and L. Oberbeck, "Deposition temperature effect on electrical properties and interface of high-*k* ZrO2 capacitor," *J. Phys. D, Appl. Phys.*, vol. 41, no. 17, p. 172005, Sep. 2008, doi: 10.1088/0022-3727/41/17/172005.

[34] W. Weinreich, K. Seidel, J. Sundqvist, M. Czernohorsky, and P. Kücher, "Effect of different PDAs and a PMA on the electrical performance of TiN/ZAZ/TiN MIM capacitors," in *Proc. Int. Semiconductor Conf. Dresden-Grenoble (ISCDG)*, 2012, pp. 227–230, doi: 10.1109/ISCDG.2012.6360010.

[35] K.-W. Ang *et al.*, "Effective Schottky Barrier Height modulation using dielectric dipoles for source/drain specific contact resistivity improvement," in *IEDM Tech. Dig.*, Dec. 2012, pp. 18.6.1–18.6.4, doi: 10.1109/IEDM.2012.6479068.

[36] Z. Li *et al.*, "Flatband voltage shift of ruthenium gated stacks and its link with the formation of a thin ruthenium oxide layer at the ruthenium/dielectric interface," *J. Appl. Phys.*, vol. 101, no. 3, p. 34503, Feb. 2007, doi: 10.1063/1.2429730.

[37] H. K. Kim, I.-H. Yu, J. H. Lee, and C. S. Hwang, "Interfacial dead-layer effects in Hf-silicate films with Pt or RuO$_2$ gates," *ACS Appl. Mater. Interfaces*, vol. 5, no. 14, pp. 6769–6772, Jul. 2013, doi: 10.1021/am401842h.

[38] H. K. Kim, I.-H. Yu, J. H. Lee, T. J. Park, and C. S. Hwang, "Scaling of equivalent oxide thickness of atomic layer deposited HfO$_2$ film using RuO$_2$ electrodes suppressing the dielectric dead-layer effect," *Appl. Phys. Lett.*, vol. 101, no. 17, p. 172910, Oct. 2012, doi: 10.1063/1.4764541.

[39] S. Y. Lee *et al.*, "Investigation of ultrathin Pt/ZrO$_2$−Al$_2$O$_3$−ZrO$_2$/TiN DRAM capacitors Schottky barrier height by internal photoemission spectroscopy," *Current Appl. Phys.*, vol. 17, no. 2, pp. 267–271, Feb. 2017, doi: 10.1016/j.cap.2016.12.004.

[40] G. Jegert, A. Kersch, W. Weinreich, and P. Lugli, "Ultimate scaling of TiN/ZrO$_2$/TiN capacitors: Leakage currents and limitations due to electrode roughness," *J. Appl. Phys.*, vol. 109, no. 1, p. 14504, Jan. 2011, doi: 10.1063/1.3531538.

[41] D. Zhou *et al.*, "Reliability of Al$_2$O$_3$-doped ZrO$_2$ high-k dielectrics in three-dimensional stacked metal-insulator-metal capacitors," *J. Appl. Phys.*, vol. 108, no. 12, p. 124104, Dec. 2010, doi: 10.1063/1.3520666.

[42] G. Jegert, A. Kersch, W. Weinreich, and P. Lugli, "Monte Carlo simulation of leakage currents in TiN/ZrO$_2$/TiN capacitors," *IEEE Trans. Electron Devices*, vol. 58, no. 2, pp. 327–334, Feb. 2011, doi: 10.1109/TED.2010.2090158.

[43] G. Jegert, D. Popescu, P. Lugli, M. J. Häufel, W. Weinreich, and A. Kersch, "Role of defect relaxation for trap-assisted tunneling in high-k thin films: A first-principles kinetic Monte Carlo study," *Phys. Rev. B, Condens. Matter*, vol. 85, no. 4, p. 45303, Jan. 2012, doi: 10.1103/PhysRevB.85.045303.

[44] Y. Seo, S. Lee, I. An, C. Song, and H. Jeong, "Conduction mechanism of leakage current due to the traps in ZrO$_2$ thin film," *Semicond. Sci. Technol.*, vol. 24, no. 11, p. 115016, Nov. 2009, doi: 10.1088/0268-1242/24/11/115016.

[45] W. Jeon *et al.*, "Evaluating the top electrode material for achieving an equivalent oxide thickness smaller than 0.4 nm from an Al-Doped TiO2 film," *ACS Appl. Mater. Interfaces*, vol. 6, no. 23, pp. 21632–21637, Dec. 2014, doi: 10.1021/am506677e.

[46] K. C. Chiang *et al.*, "High-temperature leakage improvement in metal–insulator–metal capacitors by work–function tuning," *IEEE Electron Device Lett.*, vol. 28, no. 3, pp. 235–237, Mar. 2007, doi: 10.1109/LED.2007.891265.

[47] A. Paskaleva *et al.*, "Influence of the amorphous/crystalline phase of Zr$_{1−x}$AlxO$_2$ high-k layers on the capacitance performance of metal insulator metal stacks," *J. Appl. Phys.*, vol. 106, no. 5, p. 054107, Sep. 2009, doi: 10.1063/1.3204666.

[48] W. Jeon *et al.*, "Asymmetry in electrical properties of Al-doped TiO$_2$ film with respect to bias voltage," *Phys. Status Solidi, Rapid Res. Lett.*, vol. 9, no. 7, pp. 410–413, Jul. 2015, doi: 10.1002/pssr.201510146.

[49] W. Jeon *et al.*, "Chemistry of active oxygen in RuO$_x$ and its influence on the atomic layer deposition of TiO$_2$ films," *J. Mater. Chem. C*, vol. 2, no. 46, pp. 9993–10001, Oct. 2014, doi: 10.1039/C4TC01381F.

[50] A. Chaker, P. D. Szkutnik, J. Pointet, P. Gonon, C. Vallée, and A. Bsiesy, "Understanding the mechanisms of interfacial reactions during TiO$_2$ layer growth on RuO$_2$ by atomic layer deposition with O$_2$ plasma or H$_2$O as oxygen source," *J. Appl. Phys.*, vol. 120, no. 8, p. 85315, Aug. 2016, doi: 10.1063/1.4960139.

[51] A. Sinhamahapatra, J.-P. Jeon, J. Kang, B. Han, and J.-S. Yu, "Oxygen-deficient zirconia (ZrO$_{2−x}$): A new material for solar light absorption," *Sci. Rep.*, vol. 6, Jun. 2016, Art. no. 27218, doi: 10.1038/srep27218.

Youngjin Kim received the bachelor's and M.Sc. degrees in chemical engineering from Kyonggi University, Suwon, South Korea, in 2010 and 2012, respectively. He is currently pursuing the Ph.D. degree in NBIT convergence with the Graduate School of Converging Science and Technology, Korea Institute of Science and Technology (KIST), Korea University, Seoul, South Korea.

From 2012 to 2013, he was a Research Scientist with KIST.

Cheol Hyun An received the bachelor's degree in materials science and engineering from Seoul National University, Seoul, South Korea, in 2013, where he is currently pursuing the Ph.D. degree in materials science and engineering.

His current research interests include atomic layer deposition of novel metal electrode of the metal–insulator–metal capacitors, and growth and properties of atomic layer deposited Ru noble metal.

Cheol Seong Hwang received the Ph.D. degree from Seoul National University, Seoul, South Korea, in 1993.

Since 1998, he has been a Professor with the Department of Materials Science and Engineering, Seoul National University. His current research interests include high-k gate oxides, dynamic random access memory capacitors, new memory devices including resistive RAM devices and ferroelectric materials and devices, energy storage capacitors, and neuromorphic computing.

Patrice Gonon received the Ph.D. degree in physics from Joseph Fourier University, Grenoble, France, in 1993.

He is currently serving as an associate professor, teaching electricity, semiconductor materials, and microelectronics technology with the Microelectronics Technology Laboratory, Grenoble Alpes University. From 1993 to 1994, he was a Post-Doctoral Fellow with the Fraunhofer Institute, Freiburg, Germany.

Woojin Jeon received the bachelor's and M.Sc. degrees in materials science and engineering from the Korea Advanced Institute of Science and Technology, Daejeon, South Korea, in 2005 and 2007, respectively, and the Ph.D. degree in materials science and engineering from Seoul National University, Seoul, South Korea, in 2015.

He is currently a Technical Staff Member with the National Center for Scientific Research, Grenoble, France.

Christophe Vallée received the Ph.D. degree in physics from the University of Nantes, Nantes, France, in 1999. His Ph.D. dissertation focused on the plasma-enhanced chemical vapor deposition of SiO$_2$ materials from organosilicon precursors in helicon plasma reactor.

He is currently serving as a full professor with the Microelectronics Technology Laboratory, Grenoble Alpes University, Grenoble, France.